PNAS Nexus

PNAS Nexus, 2022, **1**, 1–11
https://doi.org/10.1093/pnasnexus/pgac269
Research Report

Tilt-induced polar order and topological defects in growing bacterial populations

Takuro Shimaya and Kazumasa A. Takeuchi*

Department of Physics, The University of Tokyo, 7-3-1 Hongo, Bunkyo-ku, 113-0033 Tokyo, Japan
*To whom correspondence should be addressed: Email: kat@kaztake.org
Edited By: Peter Fratzl

Abstract

Rod-shaped bacteria, such as *Escherichia coli*, commonly live forming mounded colonies. They initially grow two-dimensionally on a surface and finally achieve three-dimensional growth. While it was recently reported that three-dimensional growth is promoted by topological defects of winding number +1/2 in populations of motile bacteria, how cellular alignment plays a role in nonmotile cases is largely unknown. Here, we investigate the relevance of topological defects in colony formation processes of nonmotile *E. coli* populations, and found that *both* ±1/2 topological defects contribute to the three-dimensional growth. Analyzing the cell flow in the bottom layer of the colony, we observe that +1/2 defects attract cells and −1/2 defects repel cells, in agreement with previous studies on motile cells, in the initial stage of the colony growth. However, later, cells gradually flow toward −1/2 defects as well, exhibiting a sharp contrast to the existing knowledge. By investigating three-dimensional cell orientations by confocal microscopy, we find that vertical tilting of cells is promoted near the defects. Crucially, this leads to the emergence of a polar order in the otherwise nematic two-dimensional cell orientation. We extend the theory of active nematics by incorporating this polar order and the vertical tilting, which successfully explains the influx toward −1/2 defects in terms of a polarity-induced force. Our work reveals that three-dimensional cell orientations may result in qualitative changes in properties of active nematics, especially those of topological defects, which may be generically relevant in active matter systems driven by cellular growth instead of self-propulsion.

Keywords: bacteria, active nematics, topological defect, colony growth

Significance Statement:

Biofilms are three-dimensional dense aggregates of bacteria that cause various problems from industry to daily life. Using nonmotile growing *Escherichia coli*, we discovered that topological defects, i.e., locations of misalignment in cell orientation, attract cells, and promote local 3D growth. Regarding the two types of defects labeled "±1/2," while previous studies showed that only +1/2 defects attract cells, we found that −1/2 defects also become attractive in growing nonmotile bacteria. We revealed that this is realized by 3D cell tilting around defects, which leads to the emergence of a polar order and generates a polarity-induced force. These may be characteristic of growing active matter without self-propulsion of constituent particles, with possible implications for the morphogenesis of various cell populations and tissues.

Introduction

Numerous species of bacteria live in dense populations, which often take the form of biofilms (1). Besides being a challenging subject for biologists and physicists, because biofilms cause a variety of problems in medicine, industry, and our daily life (2, 3), understanding the mechanism of biofilm formation is a crucial mission across diverse disciplines. In the early stage of biofilm formation processes, two-dimensional colonies are first formed, then a three-dimensional structure is eventually constructed (1). Because mechanical interactions between cells are important at this stage, many studies have attempted to understand structure formation dynamics from a physical perspective (4).

In particular, rod-shaped bacteria, irrespective of whether they are motile or not, are aligned with each other and behave like an active nematic liquid crystal in a dense two-dimensional space (5–13). For motile bacteria, it has recently been reported that +1/2 topological defects promote three-dimensional growth of *Myxococcus xanthus* populations (13). Besides bacteria, it is known that topological defects also play decisive roles in various kinds of cell populations (14, 15), such as epithelial cells (16), neural stem cells (17), fibroblasts (18, 19), and actin fibers in *Hydra* (20). However, for growing but nonmotile bacteria, while some studies investigated how nonmotile cells initiate three-dimensional growth (21–30), the relevance of local cell alignment to three-dimensional growth, in particular, that of topological defects, remains unknown.

Here, by observing colony formation processes of nonmotile *Escherichia coli* between a coverslip and a nutrient agar pad [Fig. 1(a)], we find an indication that both +1/2 and −1/2 topological defects promote three-dimensional growth of colonies. This finding is put on solid ground by analyses of the two-dimensional

Competing Interest: The authors declare no competing interest.
Received: July 18, 2022. **Accepted:** November 30, 2022

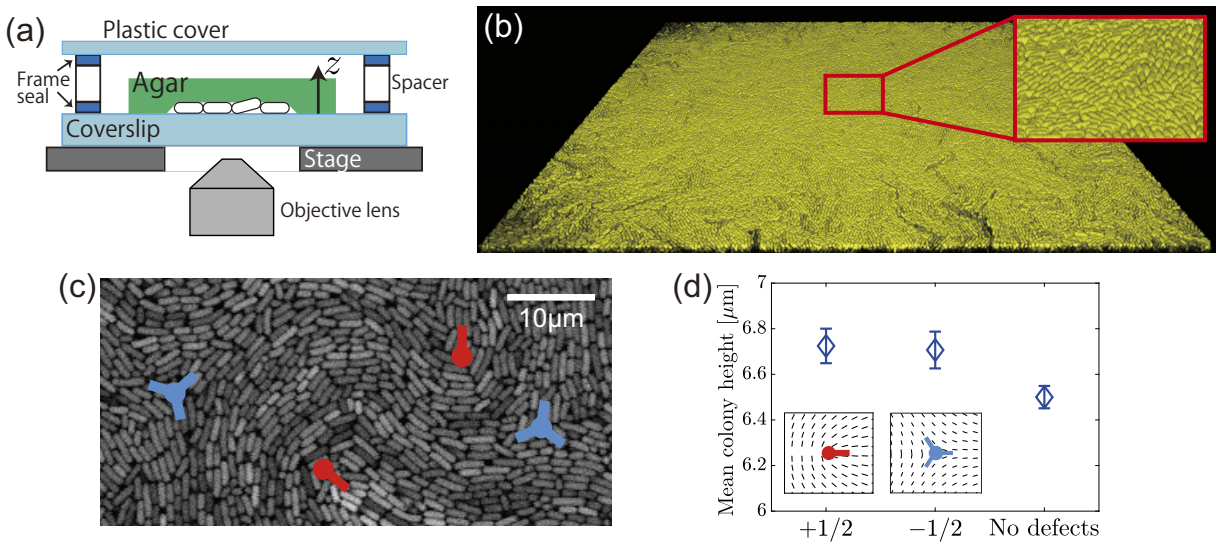

Fig. 1. Morphology of three-dimensional colonies formed from numerous cells observed by end-point confocal microscopy. The confocal data were taken 14 hours after the cells had filled the bottom plane. (a) Experimental setup. Bacterial cells were between a coverslip and a nutrient agar pad. (b) A three-dimensional image of colonies (184.52 × 184.52 μm^2), where cells were stacked three-dimensionally. The region surrounded by the red rectangle is enlarged and displayed in the upper right side. (c) A two-dimensional cross-section showing the bottom layer. Red comets and blue trefoils indicate +1/2 and −1/2 defects, respectively. The arms of the symbols reflect the structure of the director field as illustrated in the insets of (b). (d) Mean colony height at the location of the defects in the bottom layer and that far from defects. At each position in the xy-plane, the height was evaluated by the length of the profile along the z-axis whose intensity is higher than 20% of the maximum. The heights at the defect positions were extracted from all of the hundreds of defects that were sufficiently far (>9 μm) from each other. For the colony heights far from defects, we randomly picked up 1000 points, which were sufficiently far (>9 μm) from any defect (see the experimental methods discussed in Appendix A). The error bars indicate the standard error from the ensemble averaging. The optical resolution was about 250 nm in the vertical direction; see also Fig. S2(a) to (c) for the colony height distributions. Here, we show the result of a single measurement (uniform colony, end-point confocal #1); see Fig. S2(e) for the result of another biological replicate (uniform colony, end-point confocal #2), where we confirmed that the colony height was again higher at the locations of the defects.

velocity field around topological defects, which reveal that cells are transported toward both +1/2 and −1/2 defects, albeit weakly, implying upward growth there. Remarkably, this influx toward both types of defects is contrary to the existing knowledge that cells escape from −1/2 defects (5, 6, 13, 16, 17, 19), and cannot be explained by the conventional active nematic theory. Combining confocal observations and theoretical modeling, we find that the three-dimensional tilting of cells is promoted around topological defects, which can induce additional force around defects. Crucially, we uncover the formation of a polar order due to three-dimensional asymmetric tilting of cells around defects, which turns out to be the key to theoretically account for the emergence of the influx toward −1/2 defects.

Results

Topological defects promote three-dimensional growth of bacterial colonies

First, we studied the relation between cell orientation and colony structure, using nonmotile *E. coli* placed between a coverslip and a nutrient agar pad [Fig. 1(a); see the experimental methods discussed in Appendix A]. We put cell suspension on the coverslip so that cells are initially distributed densely and uniformly. Then, we cultured it for 14 hours after cells had filled the bottom plane and observed the resulting three-dimensional colony, which consisted of multiple layers of tilted cells, by confocal microscopy. Here, we took only a single confocal image at this end point, to take a high-quality image without photobleaching.

To test the relevance of cell alignment to the three-dimensional growth, we investigated whether the presence of topological defects influenced the colony height. First, we noticed that the orientation of cells in the bottom layer was nearly horizontal [Fig. 1(b) and (c)], tilted only weakly [typically ∼10° in this end-point observation; see Fig. 3(a) and descriptions thereof], and many topological defects were observed. We also observed subsequent layers and found that the cell orientation therein was essentially guided by that of the bottom layer [Fig. S1(c) to (e)]. This led us to focus on the bottom layer and regard it as a quasi-two-dimensional active nematic system. We measured the two-dimensional orientation of cells, $\boldsymbol{n}(\boldsymbol{R})$ at position $\boldsymbol{R}$ in the bottom layer, from the image intensity using the structure tensor method [see Fig. S1(a) and the experimental methods discussed in Appendix A). We then detected topological defects [Figs. 1(c) and S1], and measured the colony height at the positions of the defects (see the experimental methods discussed in Appendix A). For comparison, we also measured the colony height at randomly selected locations that are sufficiently far from topological defects. We found that the mean colony height is slightly higher at the positions of the defects [Fig. 1(d)], both +1/2 and −1/2, than in the regions far from the defects. The statistical significance is confirmed by the Wilcoxon rank-sum test (Fig. S2). For the null hypothesis that the median of the height distribution at the positions of the defects is identical to that far from defects, the P-value was 0.018 for the +1/2 defects and 0.043 for the −1/2 defects. While these results were obtained from observations of 20 separate regions in a single experiment, the reproducibility was also confirmed by another biological replicate using a different substrate and agar pad [Fig. S2(e)]. These results suggest that topological defects promote the vertical growth of colonies, slightly but statistically significantly.

Two-dimensional velocity fields around topological defects

To clarify the origin of the promoted three-dimensional growth, we investigate how cells in the bottom layer were displaced near

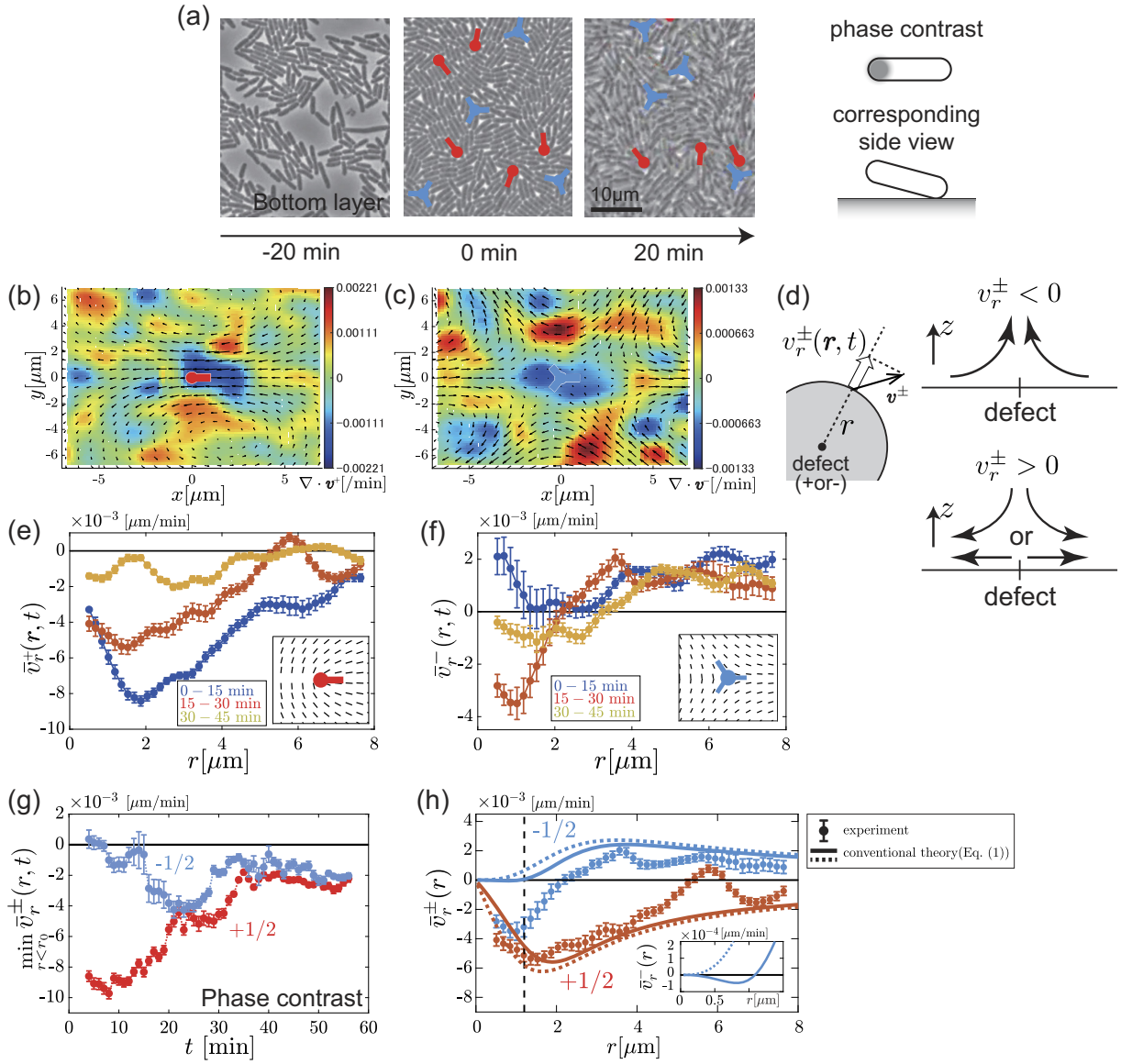

Fig. 2. Phase-contrast images and results of two-dimensional velocity analyses for uniform colonies formed from numerous cells observed by phase-contrast microscopy. The time interval of the time-lapse observation was 1 min. The double sign ± corresponds to the sign of the defects. These data were obtained by a single measurement (uniform colony, phase contrast #1), but the reproducibility was confirmed in Fig. S5 by using another biological replicate with a different substrate and agar pad (uniform colony, phase contrast #2). (a) Phase-contrast images of cells taken at $t = -20$, 0, 20 min, from left to right. $t = 0$ is the moment when cells filled the bottom plane; see also Videos 1 and 2. The sketches on the right side illustrate how three-dimensionally tilted cells appear in the phase-contrast images. (b and c) Velocity field $\boldsymbol{v}^{\pm}(\boldsymbol{r})$ (black arrows) and its divergence (color map) around +1/2 defects (b) and −1/2 defects (c). (d) Schematic illustration of the definition of the radial velocity $v_r^{\pm}(\boldsymbol{r}, t)$. With this, the mean radial velocity is defined by $\bar{v}_r^{\pm}(r, t) \equiv \frac{1}{2\pi}\oint d\phi v_r^{\pm}(\boldsymbol{r}, t)$, which corresponds to the average of the radial components of the velocity over a circumference of radius r centered at the defect. The sign of $\bar{v}_r^{\pm}$ indicates the direction of net flow, including the existence of vertical growth if $\bar{v}_r^{\pm} < 0$. (e and f) Time evolution of the mean radial velocity $\bar{v}_r^{\pm}(r, t)$ around +1/2 defects (e) and −1/2 defects (f). Here, we used the velocity field averaged over 0 min ≤ t ≤ 15 min, 15 min ≤ t ≤ 30 min, and 30 min ≤ t ≤ 45 min. The error bars indicate the time average of the standard error evaluated from each frame. (g) Time evolution of the minimum of $\bar{v}_r^{\pm}(r, t)$ in the region $r < r_0 = 2\ \mu$m near the defect. The moving average taken from (t − 5 min) to (t + 5 min) is shown with the corresponding error bar. (h) Comparison of the mean radial velocity $\bar{v}_r^{\pm}(r)$ between the experimental data (symbols) and theoretical curves based on the conventional equation (Eq. 1) (lines). The displayed experimental data (symbols) are identical to those shown in (e and f) for 15 min ≤ t ≤ 30 min (for which the influx toward −1/2 defects was strongest). The vertical dashed lines indicate the defect core radius [see Fig. S6(a) and (b)]. The dotted lines represent the results for $\epsilon = \epsilon_0$ and $a_n = a_n^0$ ($\epsilon = 0.25$, $a_n/\xi_0 = 0.055\ \mu\text{m}^2/\text{min}$, $r_S = 1.2\ \mu$m; see Appendix B), which correspond to the conventional case of extensile active nematics. The solid lines are the results for Eq. (1) with three-dimensional nematic tilting, i.e., $a_n = a_n^0 \cos\theta_n^{\pm}(\boldsymbol{r})$. Specifically, we used $\theta_n^{\pm}(r, \phi) = \theta_n^{\infty} + (\theta_n^0 - \theta_n^{\infty})\exp(-r^2/r_\theta^2)$ with $\theta_n^{\infty} = 0.3$ and $\theta_n^0 = 0.75$, with the other parameters left unchanged (see Appendix B). The inset is a close-up of the results for −1/2 defects.

topological defects. We conducted a time-lapse phase-contrast observation of the bottom layer of cells, cultured from densely and uniformly distributed populations as in the confocal observation (see the experimental methods discussed in Appendix A). Cells then filled the two-dimensional plane rather homogeneously, without forming visible microcolonies, and after a short while, cells started to tilt upward, almost simultaneously [Fig. 2(a) and Video 1; the appearance of a dark spot in the cell body indicates the tilting of the cell, as sketched in Fig. 2(a)]. Based on the uniformity of this initial two-dimensional growth, as compared

to the growth of a single circular colony discussed later, we shall refer to the present case as "uniform colony" in the following. Using the images after the two-dimensional plane was filled, we detected topological defects from the two-dimensional cell orientation $\boldsymbol{n}(\boldsymbol{R}, t)$ of the bottom layer, where $t \geq 0$ is the time elapsed since the bottom plane was filled. The density of defects initially increased slightly, then stayed approximately constant from $t \approx$ 30 min [Fig. S3(a)]. As expected from the absence of cell motility, the defects moved only a little in our system, typical displacements being a few microns over the observation time [Fig. S3(b)].

We then measured the velocity field around defects by particle image velocimetry (PIV) (see the experimental methods discussed in Appendix A). In Fig. 2(b) and (c), the arrows show the velocity field $\boldsymbol{v}^{\pm}(\boldsymbol{r}, t)$ around ±1/2 defects, time-averaged over 30 min $\leq t \leq$ 105 min, where $\boldsymbol{r}$ indicates the position relative to the defect and the double sign corresponds to the sign of the defect [see also Fig. S4(a) and (b)]. While the structure of $\boldsymbol{v}^{\pm}(\boldsymbol{r}, t)$ resembles those around defects in typical extensile active nematic systems (31), their divergence $\nabla \cdot \boldsymbol{v}^{\pm}(\boldsymbol{r}, t)$ [Fig. 2(b) and (c); see also Fig. S4(e)] reveals a distinguished character of our system: we found negative divergence around both types of defects, not only around +1/2 defects [Fig. 2(b)] as previously reported for systems of motile cell populations (5, 6, 13, 16, 17, 19), but even around −1/2 defects [Fig. 2(c)], as opposed to those earlier studies. Since negative divergence indicates influx of cells, this implies that cells are moving toward both types of defects in the bottom layer and pushed out upward. This is consistent with the result of the confocal observation that the colony height was higher at the positions of the ±1/2 defects. To inspect the time evolution of this influx, we examined the mean radial velocity at a distance r from +1/2 or −1/2 defect, $\bar{v}_r^{\pm}(r, t) \equiv \frac{1}{2\pi} \oint d\phi v_r^{\pm}(\boldsymbol{r}, t)$, where $v_r^{\pm}(\boldsymbol{r}, t)$ is the radial component of the velocity $\boldsymbol{v}^{\pm}(\boldsymbol{r}, t)$ at polar coordinates $\boldsymbol{r} = (r, \phi)$ centered at the defect [Fig. 2(d)]. For the +1/2 defects [Fig. 2(e)], we find that $\bar{v}_r^{+}(r)$ is essentially negative all the time, but the depth of the minimum decreased with increasing time. This may be because of decay of the overall flow speed throughout the colony [Fig. S4(f)], possibly due to nutrient starvation, pressure increase, and/or quorum sensing. In contrast, for the −1/2 defects [Fig. 2(f)], $\bar{v}_r^{-}(r)$ was initially positive for all r, but decreases near the defect and eventually becomes negative. To see the time-dependent influx toward the defects more clearly, we plotted $\min_{r<r_0} \bar{v}_r^{\pm}(r)$ with $r_0 = 2$ μm in Fig. 2(g). While the strength of the influx toward the +1/2 defect monotonically decreased, that toward the −1/2 defect increased until $t \simeq 25$ min. These suggest an intrinsic change in the dynamics around the −1/2 defect that cannot be explained by the decay of the overall flow speed. The reproducibility was confirmed by an independent biological replicate (Fig. S5). Although the strength of the influx toward −1/2 defects is weak [roughly 4×10^{-3} μm/min lasting over 15 min; see Fig. 2(f) and S5(b)], it is consistent with the amount of the increment in the colony height we observed [Fig. 1(d)]. As it is reproducible and not understandable with the current knowledge of active nematics, this led us to seek for a possible mechanism of the influx toward −1/2 defects.

Theoretical analyses and relevance of three-dimensional tilting of cells

To account for the observed influx toward −1/2 defects, we developed a theory based on two-dimensional extensile active nematics, extended to incorporate characteristics of growing nonmotile colonies we observed. Following earlier studies (7, 9, 13, 17), we describe the cell alignment by the nematic order tensor $\mathbf{Q}(\boldsymbol{r}, t) \equiv S(2\boldsymbol{n} \otimes \boldsymbol{n} - \mathbf{1})$, with the scalar nematic order parameter $S(\boldsymbol{r}, t)$, the director field $\boldsymbol{n}(\boldsymbol{r}, t)$, and the identity matrix $\mathbf{1}$ (see Appendix B). As a result of cell growth along the long axis of the cell body, interacting with nearby cells, cells exert the extensile active stress $\boldsymbol{\sigma} = -a_n \mathbf{Q}$ with the active stress coefficient $a_n (> 0)$ even without the motility (7, 9). This stress induces the force $\boldsymbol{f} = \nabla \cdot \boldsymbol{\sigma}$ and drives the velocity field $\boldsymbol{v}(\boldsymbol{r}, t)$. In the overdamped and low Reynolds number limit, this active force is balanced by the friction originating from cell–substrate interaction, giving the following linearized equation:

$$\boldsymbol{\xi v} = \nabla \cdot (-a_n \mathbf{Q}), \tag{1}$$

with the friction tensor $\boldsymbol{\xi}$. We assume that the friction is anisotropic with respect to the cell alignment: $\boldsymbol{\xi} = \xi_0(\mathbf{1} - \epsilon \mathbf{Q})$ with the friction anisotropy parameter ϵ. As suggested in ref. (32), we may reasonably assume that it is easier for *E. coli* cells to slide along their longitudinal axis, hence, $\epsilon > 0$. Setting $\mathbf{Q}$ with the theoretical director configuration for ±1/2 defects, $\boldsymbol{n}^{\pm}(\boldsymbol{r}) = (\cos(\pm\phi/2), \sin(\pm\phi/2))$ with azimuth ϕ of the coordinate $\boldsymbol{r}$, and using the experimentally determined core radius [see Appendix B and Fig. S6(a) and (b)], we calculated the mean radial velocity $\bar{v}_r^{\pm}(r)$ (Supplementary Information, Section I) and display the curves in Fig. 2(h) (dotted lines). Being consistent with the literature (13, 17), this shows influx only for +1/2 defects ($\bar{v}_r^{+}(r) \leq 0$) and outflux only for −1/2 defects ($\bar{v}_r^{-}(r) \geq 0$). Therefore, to explain the experimentally observed influx toward −1/2 defects, we need to extend the existing theoretical framework described so far. At this point, it is useful to remark that $\frac{d\bar{v}_r^{-}}{dr}(0) = 0$, while $\frac{d\bar{v}_r^{+}}{dr}(0) < 0$ [see Eq. (S7) in Supplementary Information], so that the curve $\bar{v}_r^{-}(r)$ for −1/2 defects stays near zero for small r [blue dotted line in Fig. 2(h)]. Therefore, even a minor effect may be sufficient to change the sign of $\bar{v}_r^{-}(r)$ near the defects. One may consider that it might be the density heterogeneity, in particular small voids observed at −1/2 defects in the early stage of the process (Video 1). However, this is unlikely to explain the observed influx, because more voids existed at earlier times whereas the influx developed later [compare Video 1 and Fig. 2(g)]. We also examined the possibility that the cell growth may generate an influx toward −1/2 defects, by adding a growth term to the hydrodynamic equation, but this did not yield the influx (see Supplementary Information).

Instead of the growth and the density heterogeneity, here, we focus on the three-dimensional orientations of the cells, because the influx toward −1/2 defects became strong when cells began to tilt three-dimensionally [Fig. 2(f) and (g) and Videos 1 and 2) despite the decay of the overall flow speed. We experimentally measured the tilt angle θ_n of cells from the horizontal plane [see the illustration in Fig. 3(a)], at a late time t from the end-point confocal data, by the structure tensor method for the three-dimensional space, applied to the bottom layer (see the experimental methods discussed in Appendix A). Taking average over the regions around ±1/2 defects, we obtained a field of the tilt angle, $\theta_n^{\pm}(\boldsymbol{r})$ (Fig. 3). While almost all cells were already tilted (hence, $\theta_n^{\pm}(\boldsymbol{r}) > 0$ everywhere) at the moment of the end-point observation, we found that three-dimensional tilting was strongest at the core of both defects [Fig. 3; see also Fig. S7(a) and (b) for the results of another biological replicate]. The peak of $\theta_n^{\pm}(\boldsymbol{r})$ is well approximated by a Gaussian function centered at the defect core plus a constant [Fig. 3(a)], and $\theta_n^{\pm}(\boldsymbol{r})$ turned out to be essentially isotropic [Fig. 3(b) and (c)].

We considered that this tilting may have weakened, in our two-dimensional description, the local active stress and the friction anisotropy around the defects. More quantitatively, we assume that the local active stress coefficient and the friction anisotropy

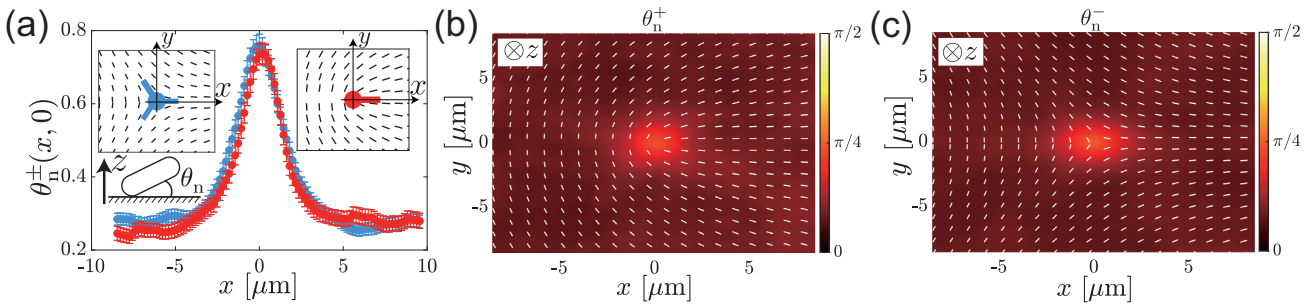

Fig. 3. Results on the three-dimensional nematic tilting obtained by the end-point confocal observation. To obtain them, we first measured the three-dimensional cell orientations by the structure tensor method and obtained the nonnegative tilt angle with respect to the *xy*-plane (see the experimental methods discussed in Appendix A). We then took the ensemble average over all defects. These data were obtained by a single measurement (uniform colony, end-point confocal #1), but the reproducibility was confirmed in Fig. S7(a) and (b) by using another biological replicate with a different substrate and agar pad (uniform colony, end-point confocal #2). (a) Nematic tilt angle $\theta_n^{\pm}(\boldsymbol{r})$ around ±1/2 defects. The results on the x-axis, i.e., $\boldsymbol{r} = (x, 0)$, are displayed. The error bars indicate the standard error from the ensemble averaging. The two insets illustrate the definition of the axes for +1/2 (right inset) and −1/2 (left inset) defects. (b and c) Spatial profiles of the nematic tilt angle $\theta_n^{\pm}(\boldsymbol{r})$ for the +1/2 defects (b) and the −1/2 defects (c). The white rods represent the nematic director field.

are given by $a_n(\boldsymbol{r}, t) = a_n^0 \cos\theta_n(\boldsymbol{r}, t)$ and $\epsilon(\boldsymbol{r}, t) = \epsilon_0 \cos\theta_n(\boldsymbol{r}, t)$, respectively, with constants a_n^0 and ϵ_0. Using this, we solved Eq. (1) and found that the influx toward −1/2 defects can emerge [Fig. 2(h) blue solid line and inset; see also Fig. S6(c)] within the reasonable range of parameter values. However, the strength of the influx was too small to account for the experimental result [Fig. 2(h) blue symbols, to be compared with the blue solid line]. This led us to seek for another key factor for the influx toward −1/2 defects.

Here, we propose a key mechanism for the observed influx toward −1/2 defects. So far, we assumed that active force is induced only by nematic alignment. However, when cells are tilted three-dimensionally, the sign of the tilt angle θ_p may break the nematic symmetry and make it possible to develop a polar order [Fig. 4(a)]. If this happens, the violation of the nematic symmetry may result in the generation of an additional force term that is otherwise forbidden, which needs to be included in the force balance Eq. (1). Such a polarity-induced force is expected to be proportional to the strength of the polar order, i.e., θ_p, in its lowest order, and act in the direction of the director. In this context, it is interesting to refer to past experiments on densely packed vibrated granular rods (33, 34), which indeed showed the formation of the polar order due to rod tilting and the resulting horizontal transport of the rods, driven by the polarity-induced force. This suggests that a similar polarity-induced force may arise in our growing bacterial populations, resulting from the extensile active force of cells, if the polar order is formed. Inspired by this possibility, we measured $\theta_p(\boldsymbol{r})$ around both types of defects by end-point confocal microscopy. Note that the single-cell tilt angles fluctuate largely from cell to cell (see Videos 1 and 2), and this is why θ_p and θ_n, i.e., the signed and unsigned averages of the tilt angles, respectively, differ. The sign of θ_p is determined by choosing the direction of the head of the nematic director $\boldsymbol{n}$ [see Fig. 4(a) and Appendix A]: here, we set $\boldsymbol{n}^{\pm}(\boldsymbol{r}) = (\cos(\pm\phi/2), \sin(\pm\phi/2))$ for the director field around ±1/2 defects. Figure 4(b) displays the result on the +*x*-axis. This shows nonvanishing $\theta_p(\boldsymbol{r})$ for both ±1/2 defects, specifically $\theta_p(\boldsymbol{r}) > 0$ (upper end oriented outward) for +1/2 defects and $\theta_p(\boldsymbol{r}) < 0$ (upper end oriented inward) for −1/2 defects on the +*x*-axis, demonstrating the emergence of the polar order in our growing bacterial populations. Consequently, the above-mentioned symmetry argument predicts the polarity-induced force $\boldsymbol{f}_p$ to arise, which satisfies $\boldsymbol{f}_p \propto \theta_p \boldsymbol{n}$ for small θ_p. In Fig. 4(c) and (d), we show $\theta_p^{\pm}(\boldsymbol{r})\boldsymbol{n}^{\pm}(\boldsymbol{r})$ around ±1/2 defects, which represent the strength and the direction of the polarity-induced force $\boldsymbol{f}_p(\boldsymbol{r})$. What contributes to the mean radial velocity is its radial component $f_{p,r}^{\pm}(\boldsymbol{r})$, proportional to $\theta_p^{\pm}(\boldsymbol{r})n_r^{\pm}(\boldsymbol{r})$, which is shown in Fig. 4(e) and (f), with $n_r^{\pm}(\boldsymbol{r})$ being the radial component of the director $\boldsymbol{n}^{\pm}(\boldsymbol{r})$. These results show that, while the polarity-induced force around +1/2 defects drives the defects toward their comet tail, that around −1/2 defects acts inward, leading to the influx toward the defects. We confirmed the reproducibility of the main structure of the polarity-induced force by taking a biological replicate (Fig. S7), as well as by a time-lapse confocal observation of yet another biological replicate [Fig. S8(d) and (e)].

To quantitatively deal with the effect of the polar order upon the mean radial velocity, we incorporate the polarity-induced force $\boldsymbol{f}_p$ into Eq. (1). With $a_n = a_n^0 \cos\theta_n$ and $\boldsymbol{\xi} = \xi_0(\mathbf{1} - \epsilon_0 \cos\theta_n \mathbf{Q})$, we obtain the following equation:

$$\xi_0(\mathbf{1} - \epsilon_0 \cos\theta_n \mathbf{Q})\boldsymbol{v} = \nabla \cdot (-a_n^0 \cos\theta_n \mathbf{Q}) + a_p^0 \theta_p \boldsymbol{n}. \tag{2}$$

Then, we experimentally determined $\theta_n(\boldsymbol{r}, t)$ and $\theta_p(\boldsymbol{r}, t)$ for ±1/2 defects, by combining end-point and time-lapse confocal observations (see Appendix B for details). We are to determine three unknown parameters, $a_n^0 S_0/\xi_0$, a_p^0/ξ_0, and $\epsilon_0 S_0$, where S_0 is the scalar nematic order parameter sufficiently far from defects. In the leading term, ϵ_0 appears in the form of a product with $a_n^0 S_0/\xi_0$ [see Supplementary Information, Eq. (S23) for example], so that we only need to tune $a_n^0 S_0/\xi_0$ and a_p^0/ξ_0. Then, while the nematic contribution solely could not reproduce the experimental result as we described above, we found, remarkably, that the addition of the polar contribution a_p^0/ξ_0 strengthened the influx toward −1/2 defects significantly [Fig. 4(g) solid curves]. In particular, we were able to find such values of $a_n^0 S_0/\xi_0$ and a_p^0/ξ_0 that satisfactorily reproduced the experimental data of both $\bar{v}_r^+(r)$ and $\bar{v}_r^-(r)$ simultaneously (see the experimental methods discussed in Appendix A). We tested this for all of the four pairs of the phase-contrast data sets (#1 or #2; see Table A1) and the end-point confocal data sets (#1 or #2) and found agreement of similar quality (Fig. S9). This demonstrates that the three-dimensional tilting and resulting polar order were the keys to understand the unusual influx toward −1/2 defects we observed in our growing nonmotile bacterial populations.

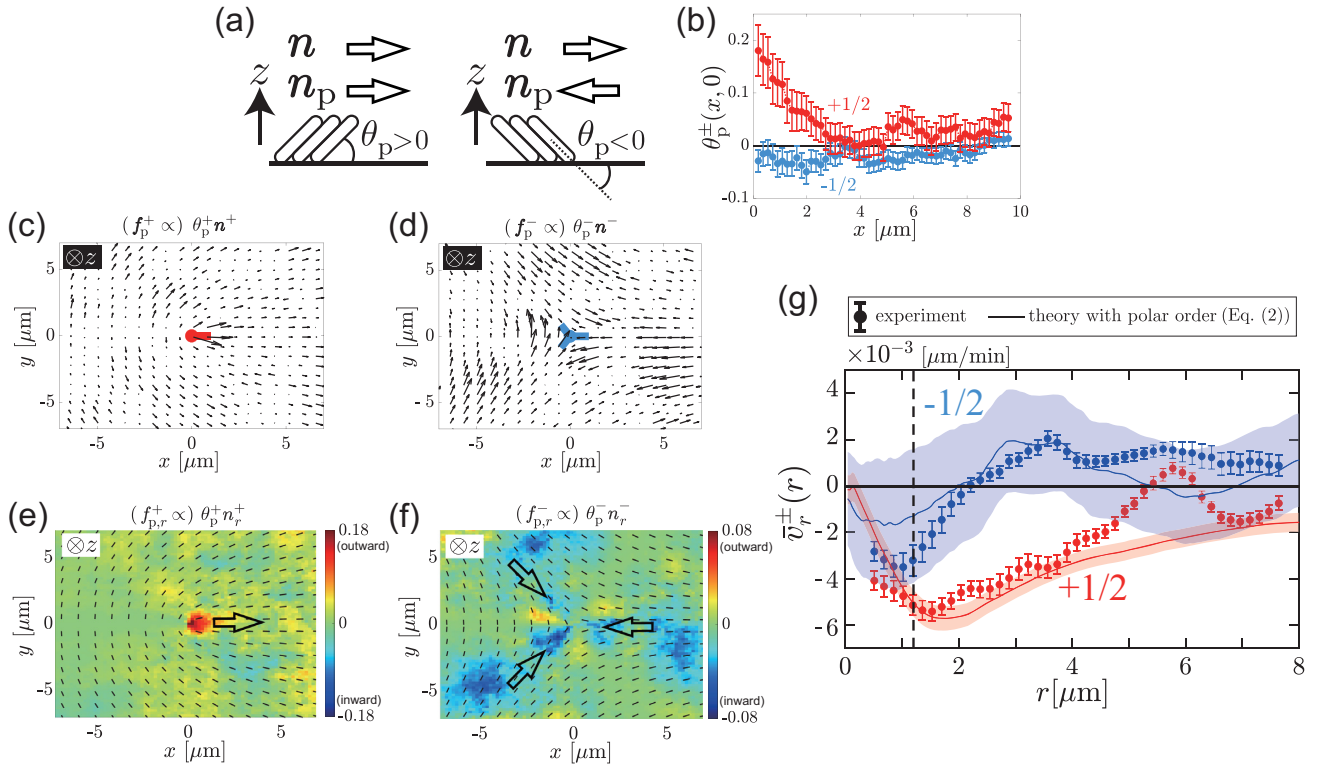

Fig. 4. Results on the polar order obtained by the single end-point confocal measurement (uniform colony, end-point confocal #1) [see also Fig. S7(c) to (g) for the results of another biological replicate (uniform colony, end-point confocal #2)] and theoretical calculations of the mean radial velocity based on our theory with polar order. (a) Illustrations of the polar tilt angle θ_p and the polar director $\boldsymbol{n}_p = \boldsymbol{n}\theta_p/|\theta_p|$. By choosing the direction of the head of the nematic director $\boldsymbol{n}$, we can uniquely determine the sign of θ_p. The polar tilt angle θ_p takes a positive (negative) value if the cell end at the head (tail) of the director $\boldsymbol{n}$ is lifted above the substrate. Note that θ_p changes its sign if $\boldsymbol{n}$ is reversed, but $\boldsymbol{n}_p$ remains unchanged, always pointing the direction of the upper end of the cell. The polarity-induced force $\boldsymbol{f}_p \propto \theta_p \boldsymbol{n}$ is oriented toward $\boldsymbol{n}_p$ (see the experimental methods discussed in Appendix A). In the following, we use $\boldsymbol{n}^{\pm} = (\cos(\pm\phi/2), \sin(\pm\phi/2))$ for the director field around $\pm 1/2$ defects, with azimuth ϕ of the coordinate $\boldsymbol{r}$. (b) The polar tilt angle $\theta_p^{\pm}$ measured on the +x-axis of $\pm 1/2$ defects [see Fig. 3(a) for the definition of the axis]. The ensemble average over all defects is shown. The error bars indicate the standard error from the ensemble averaging. (c and d) $\theta_p^{\pm}\boldsymbol{n}^{\pm}$, representing the strength and direction of the polarity-induced force $\boldsymbol{f}_p^{\pm}$ around the +1/2 defect (c) and the −1/2 defect (d). This direction indicates which ends of cells are lifted up on average. (e and f) $\theta_p^{\pm} n_r^{\pm}$, which is proportional to the radial component of the polarity-induced force, $f_{p,r}^{\pm}$, around the +1/2 defect (e) and the −1/2 defect (f). The negative radial component indicates that the polarity-induced force is directed toward the defect. The black rods represent the nematic director field. The outlined arrows illustrate the direction of the radial component of the polarity-induced force near the defect. (g) Comparison of the mean radial velocity between the experimental data (symbols) and our theoretical curves with nematic tilting and polar order (lines) (Eq. 2). The theoretical curves (lines) use the experimental data of θ_p from the end-point confocal observation #1, and the direct experimental data of the mean radial velocity (symbols) are from the phase-contrast observation #1 [those shown in Fig. 2(e) and (f)]; see Fig. S9 for the results using other data sets. The shaded bands indicate the range of uncertainty, evaluated from the standard error of the experimental data of $\theta_p^{\pm}(\boldsymbol{r}, t)$, which were directly used in the theoretical evaluation. The parameters on the nematic tilt angle were set to be $\theta_n^{\infty} = 0.2$ and $\theta_n^0 = 0.25$ on the basis of the time-lapse confocal observation data [Fig. S8(b); see Appendix B]. The other parameter values were $\epsilon_0 = 0.25$, $a_n^0/\xi_0 = 0.055\ \mu m^2/min$, and $a_p^0/\xi_0 = 0.8\ \mu m/min$ (see Appendix B). The vertical dashed lines indicate the defect core radius.

Relation to circular colonies formed from isolated cells

Although many earlier studies have already investigated how nonmotile bacteria construct three-dimensional structures, most of them have focused on the process where isolated cells grow and form circular colonies (21, 23, 24, 26, 30). In this situation, it has been reported that the in-plane stress derived from cell growth is maximized at the center of the colony (26, 35–37), which causes a few cells to be verticalized first, locally, near the center (21, 23, 26). This is contrasted to the case of our experiments starting from densely and uniformly distributed cells, in which cells were verticalized almost homogeneously and simultaneously (Video 1). We checked if cell alignment plays any role in such circular colonies (Video 3), but detected no significant correlation between the position of the first verticalization and the strength of the local orientational order (Fig. S10; see Supplementary Information, Section IV for details). Instead, we confirmed that shorter cells tend to be verticalized first [Fig. S10(e)], in agreement with the recent theory based on the torque balance (26). These suggest that, in such isolated circular colonies, the spatially nonuniform stress indeed constitutes a major contribution to the start of the three-dimensional transition, as reported earlier (21, 23, 26), regardless of topological defects. Conversely, by using uniform colonies, we reduced the effect of nonuniform stress and thereby revealed the intriguing role of topological defects in the three-dimensional transition.

Note also that a previous study (23) on circular colonies reported that collisions between colonies also triggered the cell extrusion in that case. In the case of uniform colonies from numerous cells we studied, groups of cells merged and filled holes to complete the formation of the two-dimensional bottom layer [Video 1 and Fig. S11(a)]. We tested the possible influence of such collisions upon our defect analyses, by exam-

ining whether hole filling events affected the defect formation. Detecting the locations of the holes at $t = -5$ min [Fig. S11(a)] and those of the defects at $t = 0$ [Fig. S11(b)], we confirmed that hole filling events did not promote the formation of defects [Fig. S11(c) and (d)]. Therefore, we conclude that our results on the relevance of topological defects to the cell flow and the three-dimensional growth are not significantly affected by cell collisions that preceded the formation of the complete bottom layer.

Concluding remarks

In summary, we showed the relevance of topological defects to the three-dimensional growth of growing nonmotile *E. coli* populations, unveiling the emergence of polar order and resulting novel properties endowed with this active nematic system. When cultured from densely and uniformly distributed populations, cells started to construct the three-dimensional structure a short while after they filled the bottom plane. Since then, the net influx toward both $+1/2$ and $-1/2$ defects appeared, which may have promoted the vertical growth of colonies. The influx toward $-1/2$ defects was unexpected from the existing theory of active nematics, but we revealed that this resulted from the three-dimensional tilting of cells around defects and the polar order induced thereby. We extended the active nematics theory to incorporate these effects and successfully accounted for the experimental observation.

Our results suggest the role of $-1/2$ defects in the formation of three-dimensional structures of nonmotile cell populations, which has been overlooked compared to that of $+1/2$ defects supported by many recent studies on motile cells (5, 6, 13, 16, 17, 19). Although it is fair to recall that the strength of the effects reported here, i.e., the height increase at the defects and the cell influx thereto, is not large in our setup, it is possible that vertical growth may have been prevented by the presence of the agar. Further investigation is needed to see whether the colony height above the defects can grow further, by alternative methods that can stably measure sessile *E. coli* populations for a longer period of time, and whether the orientation and topological defects in intermediate layers may also affect the colony height. Besides, it is important to contemplate the possibility of physiological significance that topological defects may ultimately have. In *Bacillus subtilis* colonies, it has been found that the roughness of the colony surface can change the wettability of the biofilm, making it more resistant to droplets that may contain toxic substances (38–42). It is therefore tempting to investigate the possibility that the local vertical growth mediated by topological defects might be involved in such surface morphology.

Finally, the emerging polar order and the influx toward $-1/2$ defects reported in this work may provide a novel characterization of nonmotile but growing active matter, contrasted with the standard active matter for self-propelled particles. As such, these results may also shed a new light on other cellular systems with three-dimensional structures. In this context, it is of great importance to elucidate how the polar order is formed when cells start to tilt. Our observations show that the direction of the polar order [Fig. 4(c) and (d)] and that of the velocity field [Fig. 2(b) and (c) arrows, typical of extensile active nematics (31)] tend to be oriented oppositely. This suggests that the polar order may be driven by the active stress originating from the nematic orientation. The recently reported instability of the in-plane orientation in extensile active nematics (43) may also be a hint. It is also important to understand how the absence of motility is involved in this mechanism; qualitatively, we may argue that the lack of cell motility would help maintain the cell tilting. Further, elucidation of the mechanism of the polar order formation and quantitative prediction of the resulting polar angle as well as the polarity-induced force are key tasks left for future studies, which will also clarify the relevance of our findings to other cellular populations.

Acknowledgments

We are grateful to S. Ramaswamy for motivating us to investigate polar order in three-dimensional orientations. We thank Y.T. Maeda and H. Salman for sharing the plasmid DNA pZA3R-EYFP and K. Inoue for producing the strain MG1655-pZA3R-EYFP. We also acknowledge discussions with K. Kawaguchi, D. Nishiguchi, M. Sano, and Y. Zushi.

Supplementary Material

Supplementary material is available at *PNAS Nexus* online.

Funding

This work is supported by KAKENHI from the Japan Society for the Promotion of Science (JSPS) (No. 19H05800, 20H00128), by KAKENHI for the JSPS Fellows (No. 20J10682), and by JST, PRESTO Grant No. JPMJPR18L6, Japan.

Authors' Contributions

T.S. and K.A.T. designed research. T.S. performed all bacterial experiments. T.S. and K.A.T. did the modeling, wrote the codes for the numerical evaluation, analyzed data, and performed the theoretical calculations. T.S. and K.A.T. wrote the manuscript.

Preprints

A preprint of this article is published at DOI:10.48550/arXiv.2106.10954.

Data Availability

The data that support the findings of this study, as well as relevant microscope images and scripts, have been deposited in Zenodo at https://doi.org/10.5281/zenodo.7388260.

References

1. Flemming H, *et al.* 2016. Biofilms: an emergent form of bacterial life. Nat Rev Microbiol. 14: 563–575.
2. Mattila-Sandholm T, Wirtanen G. 1992. Biofilm formation in the industry: a review. Food Rev Int. 8: 573–603.
3. Shirtliff M, Leid JG. 2009. The role of biofilms in device-related infections. Berlin, Heidelberg: Springer.
4. Allen RJ, Waclaw B. 2018. Bacterial growth: a statistical physicist's guide. Rep Prog Phys. 82: 016601.
5. Peng C, Turiv T, Guo Y, Wei Q, Lavrentovich OD. 2016. Command of active matter by topological defects and patterns. Science. 354: 882–885.
6. Genkin MM, Sokolov A, Lavrentovich OD, Aranson IS. 2017. Topological defects in a living nematic ensnare swimming bacteria. Phys Rev X. 7: 011029.

7. You Z, Pearce DJG, Sengupta A, Giomi L. 2018. Geometry and mechanics of microdomains in growing bacterial colonies. Phys Rev X. 8: 031065.
8. Yaman YI, Demir E, Vetter R, Kocabas A. 2019. Emergence of active nematics in chaining bacterial biofilms. Nat Commun. 10: 2285.
9. Dell'Arciprete D, *et al.* 2018. A growing bacterial colony in two dimensions as an active nematic. Nat Commun. 9: 4190.
10. Doostmohammadi A, Thampi SP, Yeomans JM. 2016. Defect-mediated morphologies in growing cell colonies. Phys Rev Lett. 117: 048102.
11. Sengupta A. 2020. Microbial active matter: a topological framework. Front Phys. 8: 184.
12. Meacock OJ, Doostmohammadi A, Foster KR, Yeomans J.M, Durham WM. 2021. Bacteria solve the problem of crowding by moving slowly. Nat Phys. 17: 205–210.
13. Copenhagen K, Alert R, Wingreen NS, Shaevitz JW. 2021. Topological defects promote layer formation in *Myxococcus xanthus* colonies. Nat Phys. 17: 211–215.
14. Saw TB, Xi W, Ladoux B, Lim CT. 2018. Biological tissues as active nematic liquid crystals. Adv Mater. 30: 1802579.
15. Doostmohammadi A, Ladoux B. 2022. Physics of liquid crystals in cell biology. Trends Cell Biol. 32(2): 140–150.
16. Saw TB, *et al.* 2017. Topological defects in epithelia govern cell death and extrusion. Nature. 544: 212–216.
17. Kawaguchi K, Kageyama R, Sano M. 2017. Topological defects control collective dynamics in neural progenitor cell cultures. Nature. 545: 327–331.
18. Duclos G, Erlenkämper C, Joanny J, Silberzan P. 2017. Topological defects in confined populations of spindle-shaped cells. Nat Phys. 13: 58–62.
19. Turiv T, *et al.* 2020. Topology control of human fibroblast cells monolayer by liquid crystal elastomer. Sci Adv. 6(20): eaaz6485.
20. Maroudas-Sacks Y, *et al.* 2021. Topological defects in the nematic order of actin fibres as organization centres of *Hydra* morphogenesis. Nat Phys. 17: 251–259.
21. Su P, *et al.* 2012. Bacterial colony from two-dimensional division to three-dimensional development. PLoS One. 7: e48098.
22. Farrell FDC, Hallatschek O, Marenduzzo D, Waclaw B. 2013. Mechanically driven growth of quasi-two-dimensional microbial colonies. Phys Rev Lett. 111: 168101.
23. Grant MAA, Wacław B, Allen RJ, Cicuta P. 2014. The role of mechanical forces in the planar-to-bulk transition in growing *Escherichia coli* microcolonies. J R Soc Interface. 11: 20140400.
24. Duvernoy M, *et al.* 2018. Asymmetric adhesion of rod-shaped bacteria controls microcolony morphogenesis. Nat Commun. 9: 1120.
25. Beroz F, *et al.* 2018. Verticalization of bacterial biofilms. Nat Phys. 14: 954–960.
26. You Z, Pearce DJG, Sengupta A, Giomi L. 2019. Mono- to multilayer transition in growing bacterial colonies. Phys Rev Lett. 123: 178001.
27. Warren MR, *et al.* 2019. Spatiotemporal establishment of dense bacterial colonies growing on hard agar. eLife. 8: e41093.
28. Hartmann R, *et al.* 2019. Emergence of three-dimensional order and structure in growing biofilms. Nat Phys. 15: 251–256.
29. Takatori SC, Mandadapu KK. 2020. Motility-induced buckling and glassy dynamics regulate three-dimensional transitions of bacterial monolayers. arXiv:2003.05618.
30. Dhar J, Thai ALP, Ghoshal A, Giomi L, Sengupta A. 2022. Self-regulation of phenotypic noise synchronizes emergent organization and active transport in confluent microbial environments. Nat Phys. 8(8): 945–951.
31. Doostmohammadi A, Ignés-Mullol J, Yeomans JM, Sagués F. 2018. Active nematics. Nat Commun. 9: 3246.
32. Doumic M, Hecht S, Peurichard D. 2020. A purely mechanical model with asymmetric features for early morphogenesis of rod-shaped bacteria micro-colony. Math Biosci Eng. 17: 6873–6908.
33. Blair DL, Neicu T, Kudrolli A. 2003. Vortices in vibrated granular rods. Phys Rev E. 67: 031303.
34. Volfson D, Kudrolli A, Tsimring LS. 2004. Anisotropy-driven dynamics in vibrated granular rods. Phys Rev E. 70:051312.
35. Volfson D, Cookson S, Hasty J, Tsimring LS. 2008. Biomechanical ordering of dense cell populations. Proc Natl Acad Sci USA. 105: 15346–15351.
36. Boyer D, *et al.* 2011. Buckling instability in ordered bacterial colonies. Phys Biol. 8: 026008.
37. Los R, *et al.* 2020. Defect dynamics in growing bacterial colonies. arXiv:2003.10509.
38. Epstein AK, Pokroy B, Seminara A, Aizenberg J. 2011. Bacterial biofilm shows persistent resistance to liquid wetting and gas penetration. Proc Natl Acad Sci USA. 108: 995–1000.
39. Trejo M, *et al.* 2013. Elasticity and wrinkled morphology of *Bacillus subtilis* pellicles. Proc Natl Acad Sci USA. 110: 2011–2016.
40. Werb M, *et al.* 2017. Surface topology affects wetting behavior of *Bacillus subtilis* biofilms. NPJ Biofilms Microbiomes. 3: 11.
41. Hayta EN, Rickert CA, Lieleg O. 2021. Topography quantifications allow for identifying the contribution of parental strains to physical properties of co-cultured biofilms. Biofilm. 3: 100044.
42. Zabiegaj D, *et al.* 2021. Wetting/spreading on porous media and on deformable, soluble structured substrates as a model system for studying the effect of morphology on biofilms wetting and for assessing anti-biofilm methods. Curr Opin Colloid Interface Sci. 53: 101426.
43. Nejad MR, Yeomans JM. 2022. Active extensile stress promotes 3D director orientations and flows. Phys Rev Lett. 128: 048001.
44. Sveen JK. 2004. An introduction to MatPIV 1.6.1. Eprint no. 2, ISSN 0809-4403. Dept. of Mathematics, University of Oslo.
45. Pismen LM. 2006 Patterns and interfaces in dissipative dynamics. Berlin, Heidelberg: Springer.
46. Pismen LM. 1999. Vortices in nonlinear fields. From liquid crystals to superfluids. from non-equilibrium patterns to cosmic strings. Oxford: Oxford University Press.

Appendix A: experimental methods

Strains, culture media, and sample setup

We used a wild-type *Escherichia coli* strain MG1655 and its mutant MG1655-pZA3R-EYFP that contains a plasmid pZA3R-EYFP expressing enhanced yellow fluorescent proteins. We used LB broth (tryptone 1 wt%, sodium chloride 1 wt%, and Yeast extract 0.5 wt%) and TB+Cm medium (tryptone 1 wt%, sodium chloride 1 wt%, and chloramphenicol 165 μg/ml). To prepare nutrient agar pads, we added agar powder to medium, solidified it by a microwave oven, then cut it into squares of size 13 × 13 mm. For each observation, we inoculated bacterial suspension on a coverslip and put an agar pad on the suspension. We then attached the following on the coverslip, surrounding the agar pad, to prevent the agar from drying out [Fig. 1(a)]: a frame seal (SLF0601, Bio-Rad), a 3D printed PLA spacer (5 mm height, hollow square, inner dimensions 14 × 14 mm and outer dimensions 22 × 22 mm), another frame seal, then a plastic cover that enclosed the inner region. Details on the strain and the culture condition in each experiment are provided below and in Table A1. The *E. coli* strains we

used did not swim at all in our experimental conditions (Videos 1, 2, and 3).

Confocal observations of uniform colonies formed from numerous cells

We used the mutant strain MG1655-pZA3R-EYFP that expresses enhanced yellow fluorescent proteins. Before the observations, we inoculated the strain from a glycerol stock into 2 ml TB+Cm medium in a test tube. After shaking it overnight at 37°C, we transferred 20 μl of the incubated suspension to 2 ml fresh TB+Cm medium and cultured it until the optical density (OD) at 600 nm wavelength reached 0.1–0.5. The bacterial suspension was finally concentrated to OD = 5 by a centrifuge, and 1 μl of the suspension was inoculated between the coverslip and the agar pad (1.5 wt% agar).

The sample was placed on the microscope stage, in a stage-top incubator maintained at 37°C. The microscope we used was Leica SP8, equipped with a 63× (N.A. 1.40) oil immersion objective and operated by Leica LasX. The data shown in Figs. 1, 3, 4, S1, and S2 were obtained by a single end-point observation, in which we cultured the colonies without excitation light until 14 hours after the cells had filled the observation area. We also show data obtained by another biological replicate with a different substrate and agar pad in Fig. S7. For each set of these data, we captured three-dimensional images of size 184.52 × 184.52 × 16 μm from 20 separate regions. The optical resolution, as evaluated by the formula of the point-spread function, was about 140 nm in the horizontal plane and 250 nm in the vertical direction. The confocal pinhole size was 0.21 Airy unit. For the data shown in Fig. S8, we carried out a single time-lapse observation and obtained images of size 184.52 × 184.52 × 6.4 μm from four separate regions with the time interval 15 min. The image pixel size was ≈0.18 μm in the xy-plane and 0.16 μm along the z-axis.

Analysis of confocal images

For each region, we chose the plane corresponding to the bottom layer and measured the two-dimensional cell orientation $\boldsymbol{n}(\boldsymbol{R})$ by the structure tensor method. The image pixel size was ≈0.18 μm. After sharpening the images by a high-pass filter, we calculated the structure tensor $J(\boldsymbol{R})$ at a given pixel $\boldsymbol{R} = (X, Y)$ by

$$J(\boldsymbol{R}) = \begin{bmatrix} [\Delta_X I, \Delta_X I]_R, & [\Delta_Y I, \Delta_X I]_R \\ [\Delta_X I, \Delta_Y I]_R, & [\Delta_Y I, \Delta_Y I]_R \end{bmatrix}, \tag{A1}$$

with the image intensity $I(X, Y)$, $\Delta_X I \equiv I(X+1, Y) - I(X-1, Y)$, $\Delta_Y I \equiv I(X, Y+1) - I(X, Y-1)$, and $[g, h]_{\boldsymbol{R}} \equiv \sum_{(X',Y')\in \mathrm{ROI}^{\ell}_{\boldsymbol{R}}} g(X', Y') h(X', Y') f^{\sigma}_{\boldsymbol{R}}(X', Y')$. Here, the summation is taken over a region of interest $\mathrm{ROI}^{\ell}_{\boldsymbol{R}}$, which is a square of size $\ell \approx 7.2$ μm (40 pixels) centered at $\boldsymbol{R}$, and $f^{\sigma}_{\boldsymbol{R}}(X', Y')$ is the Gaussian kernel defined by $f^{\sigma}_{\boldsymbol{R}}(X', Y') \equiv \exp[-\frac{(X'-X)^2+(Y'-Y)^2}{2\sigma^2}]$ with $\sigma \approx 1.8$ μm (10 pixels). Then the cell orientation $\boldsymbol{n}(\boldsymbol{R})$ is given by the eigenvector of $J(\boldsymbol{R})$ associated with the smallest eigenvalue $\lambda^{\min}(\boldsymbol{R})$. The orientation $\boldsymbol{n}(\boldsymbol{R})$ can also be represented by angle $\psi(\boldsymbol{R})$ such that $\boldsymbol{n} = \pm(\cos\psi, \sin\psi)$ with $-\pi/2 \le \psi < \pi/2$.

To detect topological defects, we first calculated the nematic order parameter by

$$S(\boldsymbol{R}) = \langle \sin 2\psi \rangle^2_{\mathrm{ROI}^{\ell}_{\boldsymbol{R}}} + \langle \cos 2\psi \rangle^2_{\mathrm{ROI}^{\ell}_{\boldsymbol{R}}}, \tag{A2}$$

where $\langle\cdot\rangle_{\mathrm{ROI}^{\ell}_{\boldsymbol{R}}}$ denotes the spatial average within $\mathrm{ROI}^{\ell}_{\boldsymbol{R}}$. Then, we located the positions of local minima of $S(\boldsymbol{R})$ as candidates of topological defect cores. For each candidate point, we calculated the topological charge $q = \frac{1}{2\pi}\oint_{\mathcal{C}} d\psi$, where $\mathcal{C}$ is a square closed path with a side of about 3.6 μm (20 pixels) centered at the candidate point. The candidate point is regarded as a topological defect if $q = \pm 1/2$, and dismissed otherwise. To determine the angle of the arm of each defect [Fig. 1(d) inset], we used the profile of $|\psi - \phi|$ on $\mathcal{C}$, where ϕ is the azimuth with respect to the defect core. A single minimum of $|\psi - \phi|$ exists for each +1/2 defect, while there are three local minima for each −1/2 defect. Each minimum point corresponds to an arm of the defect. Blue trefoils indicating −1/2 defects in Fig. 1(c) were drawn by setting one of the arms of the trefoil at the angle of the global minimum, with the other two arms added by rotating the first arm by 120°. We thereby obtained the two-dimensional locations of all defects and their signs.

To investigate the dependence of the colony height on topological defects, we picked up hundreds of isolated defects, separated by a distance longer than 9 μm from the nearest defect. For comparison, we also randomly selected 1000 points, which are separated more than 9 μm from defects. For a given position in the xy-plane, we obtained the image intensity profile along the z-axis, with the interval of z-slices being 0.16 μm. The height was then determined by the length of the region whose intensity was higher than 20% of the maximum intensity in this profile.

The three-dimensional tilting of the cells around defects was characterized as follows. First, for each defect, we rotated the confocal image horizontally so that the defect arm was orientated in the positive direction of the x-axis. For −1/2 defects, we did this rotation for each of their three arms and obtained a set of three images from each defect. Then, for each rotated confocal image $I(\boldsymbol{r})$, where $\boldsymbol{r}$ is the coordinate relative to the defect, we obtained the three-dimensional cell orientation $\boldsymbol{n}_3(\boldsymbol{r})$ by the three-dimensional version of the structure tensor method. For each pixel $\boldsymbol{r} = (x, y, z)$, which was chosen from the plane corresponding to the bottom layer in each region, we calculated the three-dimensional structure tensor:

$$J(\boldsymbol{r}) = \begin{bmatrix} [\Delta_x I, \Delta_x I]_{\boldsymbol{r}} & [\Delta_y I, \Delta_x I]_{\boldsymbol{r}} & [\Delta_z I, \Delta_x I]_{\boldsymbol{r}} \\ [\Delta_x I, \Delta_y I]_{\boldsymbol{r}} & [\Delta_y I, \Delta_y I]_{\boldsymbol{r}} & [\Delta_z I, \Delta_y I]_{\boldsymbol{r}} \\ [\Delta_x I, \Delta_z I]_{\boldsymbol{r}} & [\Delta_y I, \Delta_z I]_{\boldsymbol{r}} & [\Delta_z I, \Delta_z I]_{\boldsymbol{r}} \end{bmatrix}, \tag{A3}$$

where $\Delta_x I \equiv I(x+1, y, z) - I(x-1, y, z)$, $\Delta_y I$ and $\Delta_z I$ are defined likewise, $[g, h]_{\boldsymbol{r}} \equiv \sum_{\boldsymbol{r}'\in \mathrm{ROI}^{\ell_x,\ell_y,\ell_z}_{\boldsymbol{r}}} g(\boldsymbol{r}') h(\boldsymbol{r}') f^{\sigma}_{\boldsymbol{r}}(\boldsymbol{r}')$. Here, the summation is taken over a three-dimensional region of interest $\mathrm{ROI}^{\ell_x,\ell_y,\ell_z}_{\boldsymbol{r}}$, which is a cuboid of size $\ell_x \times \ell_y \times \ell_z$ centered at $\boldsymbol{r}$, with $\ell_x = \ell_y \approx 4.3$ μm (24 pixels) and $\ell_z \approx 3.8$ μm (24 pixels). The Gaussian kernel $f^{\sigma}_{\boldsymbol{r}}(\boldsymbol{r}')$ is defined by $f^{\sigma}_{\boldsymbol{r}}(\boldsymbol{r}') \equiv \exp[-\frac{(\boldsymbol{r}'-\boldsymbol{r})^2}{2\sigma^2}]$ with $\sigma = 2.2$ μm. Then, the three-dimensional cell orientation $\boldsymbol{n}_3(\boldsymbol{r})$ is given by the eigenvector of $J(\boldsymbol{r})$ associated with the smallest eigenvalue. The orientation $\boldsymbol{n}_3(\boldsymbol{r})$ is then represented by angles $\psi(\boldsymbol{r})$ and $\theta(\boldsymbol{r})$ such that $\boldsymbol{n}_3 = (\cos\theta\cos\psi, \cos\theta\sin\psi, \sin\theta)$ with $0 \le \psi < 2\pi$ and $-\pi/2 \le \theta < \pi/2$. As is clear from the definition, the angle $\psi(\boldsymbol{r})$ specifies the two-dimensional cell orientation $\boldsymbol{n}(\boldsymbol{r})$ by $\boldsymbol{n} = (\cos\psi, \sin\psi)$ and $\theta(\boldsymbol{r})$ indicates the angle between the three-dimensional orientation and the xy-plane. Note that $\boldsymbol{n}_3(\boldsymbol{r})$ and $-\boldsymbol{n}_3(\boldsymbol{r})$ are equivalent, so that the sign of $\boldsymbol{n}(\boldsymbol{r})$ and $\theta(\boldsymbol{r})$ can be changed simultaneously.

To investigate statistical properties of the cell tilt angle around ±1/2 topological defects, we need to define tilt angles whose sign can be determined unambiguously. The simplest choice is to take the ensemble average of $|\theta(\boldsymbol{r})|$, which can be used to detect the presence of the three-dimensional tilting. We took this average over isolated defects of each sign, separated by a distance longer than 9 μm from the nearest defect, and this defines our $\theta^{\pm}_{\mathrm{n}}(\boldsymbol{r})$. To characterize the polar order, we need an angle that can take both positive and negative values. To define such an angle, we use the director field $\boldsymbol{n}^{\pm}_{\mathrm{ref}}(\boldsymbol{r}) \equiv (\cos(\pm\phi/2), \sin(\pm\phi/2))$ around ±1/2 defects,

Table A1. List of experimental measurements in this study.

Measurement	Strain	Initial cell density	Data
uniform colony, end-point confocal #1	a mutant MG1655-pZA3R-EYFP	high	Figs. 1, 3, 4, S1, and S2
uniform colony, end-point confocal #2	a mutant MG1655-pZA3R-EYFP	high	Fig. S7
uniform colony, phase contrast #1	a wile-type MG1655	high	Fig. 2, S3, and S10
uniform colony, phase contrast #2	a wile-type MG1655	high	Fig. S5
uniform colony, time-lapse confocal #1	a mutant MG1655-pZA3R-EYFP	high	Fig. S8
circular colony, phase contrast #1	a wile-type MG1655	low	Fig. S10
circular colony, phase contrast #2	a wile-type MG1655	low	Fig. S10

with the azimuth ϕ of the position $\boldsymbol{r}$ in the xy-plane, and took the average of the field $\theta(\boldsymbol{r})\mathrm{sign}[\boldsymbol{n}^{\pm}_{\mathrm{ref}}(\boldsymbol{r})\cdot\boldsymbol{n}(\boldsymbol{r})]$ over isolated defects (with the same criterion on the distance from other defects). This is our $\theta^{\pm}_{\mathrm{p}}(\boldsymbol{r})$ which characterized the polar order. The polarity-induced force is then $\boldsymbol{f}^{\pm}_{\mathrm{p}}(\boldsymbol{r})\propto\theta^{\pm}_{\mathrm{p}}(\boldsymbol{r})\boldsymbol{n}^{\pm}_{\mathrm{ref}}(\boldsymbol{r})$. This right-hand side is shown in Fig. 4(c) and (d), and its radial component in Fig. 4(e) and (f).

Phase-contrast observation of uniform colonies formed from numerous cells

We used the wild-type strain MG1655. Before the time-lapse observation, we inoculated the strain from a glycerol stock into 2 ml LB broth in a test tube. After shaking it overnight at 37°C, we transferred 20 μl of the incubated suspension to 2 ml fresh LB broth and cultured it until OD at 600 nm wavelength reached 0.1–0.3. The bacterial suspension was finally concentrated to OD = 5 by a centrifuge, and 1 μl of the suspension was inoculated between the coverslip and the LB agar pad (1.5 wt% agar).

The sample was placed on the microscope stage, in an incubation box maintained at 37°C. The microscope we used was Leica DMi8, equipped with a 63× (N.A. 1.30) oil immersion objective and a CCD camera (Leica DFC3000G), and operated by Leica LasX. The image pixel size was ≈0.17 μm. For the data shown in Figs. 2, S3, and S10, we used a single substrate and carried out a time-lapse observation with the time interval 1 min for 30 separate regions of dimensions 110.03 × 81.97 μm. We also obtained a biological replicate using another substrate for the data shown in Fig. S5. For each region, we determined the frame at $t = 0$, i.e., the frame in which cells filled the observation area for the first time. We then measured the cell orientation $\boldsymbol{n}(\mathbf{R})$ and detected topological defects in all frames, by the method described below. We used isolated topological defects only, each separated by a distance longer than 9.5 μm from the nearest defect. As a result, we obtained hundreds of defects for each time.

Phase-contrast observation of circular colonies formed from a few cells

We used the wild-type strain MG1655. We cultured bacteria in the same way as for the observation of uniform colonies. The bacterial suspension was finally diluted to OD = 0.01, and 1 μl of the suspension was inoculated between the coverslip and the LB agar pad (2.0 wt% agar).

The imaging process and the condition during the observation were the same as those for the observation of uniform colonies. We carried out time-lapse observations with the time interval 1 min for 30 isolated colonies, which started to form from a few cells. We repeated the experiments twice using different substrates and acquired data from 60 colonies in total. From each colony, we chose the frame right before the first extrusion of a cell from the bottom layer took place. We used 60 such images from the 60 colonies for analysis. For each colony, we binarized the image, and obtained the area A by the total number of pixels, the center position by the center of mass, and the radius $R_{\max}$ by $\pi R^2_{\max} = A$, using the regionprops function of MATLAB. The first extruded cell was detected manually, by using a black spot that a tilted cell exhibits in the phase-contrast image (see Video 3). We manually labeled pixels contained in each extruded cell, and obtained the position as well as the mean and the standard deviation of the coherency over the labeled pixels (see the section "Analysis of phase-contrast images" for the method to evaluate the coherency). To obtain the spatial dependence of the coherency shown by boxplots in Fig. S10(b), we divided the space into regions bordered by concentric circles, with the radii that increased by $R/R_{\max} = 0.1$. The length of cells was evaluated manually from the major axis of each cell by using a painting software.

Analysis of phase-contrast images

Using phase-contrast images from uniform and circular colonies, we measured the two-dimensional cell orientation $\boldsymbol{n}(\mathbf{R})$ and detected topological defects, in the same manner as those for confocal observations. The image pixel size was ≈0.17 μm. The structure tensor was calculated with the ROI size $\ell \approx 6.8$ μm (40 pixels) and the characteristic length of the Gaussian filter, $\sigma \approx 1.7$ μm (10 pixels). The detection of topological defects was carried out with the closed path $\mathcal{C}$ with a side of about 3.4 μm (20 pixels), as in Fig. 2(a) and Video 2.

In addition to the cell orientation $\boldsymbol{n}(\mathbf{R})$, we also obtained the coherency parameter $C(\mathbf{R})$ defined by

$$C(\mathbf{R}) = \frac{\lambda^{\max}(\mathbf{R}) - \lambda^{\min}(\mathbf{R})}{\lambda^{\max}(\mathbf{R}) + \lambda^{\min}(\mathbf{R})}, \tag{A4}$$

with the largest eigenvalue $\lambda^{\max}(\mathbf{R})$. This quantifies the degree of the local nematic order.

For uniform colonies, we also measured the velocity field of the cells around the detected defects, by particle image velocimetry (PIV). For this, we used MatPIV (44) (open source PIV toolbox for MATLAB), with the PIV window set to be a square of size ≈2.7 μm (16 pixels). To take averages over defects, for each defect, we rotated the image so that the defect arm was oriented in the positive direction of the x-axis. For $-1/2$ defects, we did this rotation for each of their three arms, and all of the resulting velocity fields were used for the ensemble average. We thereby obtained the ensemble-averaged velocity field $\boldsymbol{v}(\boldsymbol{r}, t)$, as a function of the coordinate $\boldsymbol{r} = (x, y)$ relative to the defect, and time t.

The divergence of $\boldsymbol{v}(\boldsymbol{r}) = (u(\boldsymbol{r}), v(\boldsymbol{r}))$ was calculated as follows (here, we omit t from the argument for simplicity). We first obtained $D(\boldsymbol{r}) = \frac{u(x+1,y)-u(x-1,y)}{2\delta} + \frac{v(x,y+1)-v(x,y-1)}{2\delta}$ with the pixel size $\delta \approx$

0.17 μm. We then calculated the divergence field by

$$(\nabla \cdot \boldsymbol{v})(\boldsymbol{r}) = \frac{\sum_{(x',y')\in \mathrm{ROI}_{\boldsymbol{r}}^{\ell}} D(\boldsymbol{r}') f_{\boldsymbol{r}}^{\sigma}(x',y')}{\sum_{(x',y')\in \mathrm{ROI}_{\boldsymbol{r}}^{\ell}} f_{\boldsymbol{r}}^{\sigma}(x',y')}, \tag{A5}$$

where $\mathrm{ROI}_{\boldsymbol{r}}^{\ell}$ and the Gaussian kernel $f_{\boldsymbol{r}}^{\sigma}(x',y')$ were defined as above, but with $\ell \approx 2.7$ μm (16 pixels) and $\sigma \approx 0.68$ μm (5 pixels).

Appendix B: theoretical calculations

To theoretically account for the experimental result of the mean radial velocity $\bar{v}_r^{\pm}(r)$, in particular the influx toward $-1/2$ defects shown in Fig. 2(e) and (f), we solved the force balance equations Eqs. (1) and (2). While detailed descriptions on the solutions are given in Supplementary Material, here, we outline the theoretical assumptions and the methods to obtain the theoretical results shown in Fig. 4(g), which satisfactorily reproduced the experimental data when the influx toward $-1/2$ defects was strongest.

First, we assume the director field winding uniformly around a $+1/2$ or $-1/2$ defect, $\boldsymbol{n}^{\pm}(r,\phi) = (\cos(\pm\phi/2), \sin(\pm\phi/2))$, where (r, ϕ) is the two-dimensional polar coordinate, centered at the defect core. The nematic order tensor $\mathbf{Q}^{\pm}(r,\phi)$ is then given by

$$\mathbf{Q}^{\pm}(r,\phi) = S(r)\begin{bmatrix} \cos(\pm\phi) & \sin(\pm\phi) \\ \sin(\pm\phi) & -\cos(\pm\phi) \end{bmatrix}, \tag{B1}$$

with the scalar nematic order parameter $S(r)$ left as a free parameter. Based on the assumption that $\mathbf{Q}^{\pm}$ minimizes the nematic free energy, $S(r)$ can be theoretically expressed by the following Padé approximant (13, 45, 46):

$$S(r) = S_0 F(r/r_S), \qquad F(x) \approx x\sqrt{\frac{0.34 + 0.07x^2}{1 + 0.41x^2 + 0.07x^4}}, \tag{B2}$$

with the defect core radius r_S and $S_0 = S(\infty)$. To determine the value of r_S, we fitted Eq. (B2) to the experimental data of the coherency $C(\boldsymbol{r})$ [Fig. S6(a) and (b)] and obtained $r_S = 1.2$ μm. Note that, because the angle field $\psi(\boldsymbol{r})$ does not contain information of the defect core, the nematic order parameter evaluated by Eq. (A2) is not suitable for estimating r_S. Concerning S_0, it always appears as a product with either ϵ or a_n, so that we fix $S_0 = 1$ without loss of generality.

The case without three-dimensional cell tilting, described by Eq. (1), was already dealt with by earlier studies (13, 17). Since Eq. (1) is linear, we can readily solve it and obtain, for the mean radial velocity:

$$\bar{v}_r^{\pm}(r) = -\epsilon \frac{a_n}{\xi_0} S(r) \frac{S'(r) \pm S(r)/r}{1 - \epsilon^2 S(r)^2}. \tag{B3}$$

Then, we can show, with Eq. (B2), that it is negative for $+1/2$ defects and positive for $-1/2$ defects, for all $r > 0$ (see Supplementary Material). In Fig. 2(h), by the dotted lines, we showed $\bar{v}_r^{\pm}(r)$ for $\epsilon = 0.25$, $a_n/\xi_0 = 0.055$ μm^2/min, $r_S = 1.2$ μm.

In fact, even in the presence of three-dimensional cell tilting and polar order, i.e., in the case of Eq. (2), it is linear in $\boldsymbol{v}$ and the solution for the case of $\pm 1/2$ defects is given by

$$\boldsymbol{v}^{\pm}(r,\phi) = \xi_0^{-1}(\mathbf{1} - \epsilon_0 \cos\theta_n^{\pm}(r,\phi)\mathbf{Q}^{\pm})^{-1} \times \left[\nabla \cdot (-a_n^0 \cos\theta_n^{\pm}(r,\phi)\mathbf{Q}^{\pm}) + a_p^0 \theta_p^{\pm}(r,\phi)\boldsymbol{n}^{\pm}\right]. \tag{B4}$$

Regarding the first term that describes the contribution by nonuniform nematic tilting, we determined $\theta_n^{\pm}(r,\phi)$ by time-lapse and end-point confocal observations. Because we could not obtain clear spatial profile of $\theta_n^{\pm}(r,\phi)$ from the time-lapse observation due to photobleaching, we used high-quality, end-point confocal images to determine the spatial profile, then calibrated its amplitude by the time-lapse observation to account for the time period of interest. First, on the spatial profile, our end-point confocal observation (Fig. 3) suggests that $\theta_n^{\pm}(r,\phi) = \theta_n^{\infty} + (\theta_n^0 - \theta_n^{\infty})\exp(-r^2/r_\theta^2)$ with constants $\theta_n^{\infty}, \theta_n^0, r_\theta$, regardless of ϕ and the sign of the defect. From the spatial profile, we obtained $r_\theta = 1$ μm. For the peak height, we used time-lapse observations for 200 min $\le t \le$ 250 min, during which the influx toward $-1/2$ defects was strongest for this strain (Fig. S8a), and estimated $\theta_n^{\infty} = 0.2$ and $\theta_n^0 = 0.25$ [Fig. S8(b)].

To see the influence of the nematic tilting, we numerically calculated $\bar{v}_r^{\pm}(r)$ with $\theta_n^{\infty} = 0.3$ and $\theta_n^0 = 0.75$, which were estimated from the end-point confocal observation, without polar order [Fig. 2(h), the solid lines]. The other parameters were $\epsilon_0 = 0.25$, $a_n/\xi_0 = 0.055$ μm^2/min, and $r_S = 1.2$ μm. The strength of the influx toward $-1/2$ defects obtained thereby was smaller than the experimental result, indicating that the nematic tilting is insufficnent to quantitatively explain the influx toward $-1/2$ defects.

For the polar contribution to Eq. (B4), we determined the spatial structure of $\theta_p^{\pm}(r,\phi)$ by the end-point confocal observation [Fig. 4(c) and (d)]. Then, we calibrated the amplitude by multiplying the ratio of $\langle\theta_p^{\pm}\rangle_{0<x<10\ \mu\mathrm{m},y=0}$ from the time-lapse observation for 200 min $\le t \le$ 250 min [Fig. S8(c)] to that from the end-point observation [Fig. 4(c) and (d)].

We are finally left to determine the following parameters: ϵ_0, a_n^0/ξ_0, and a_p^0/ξ_0. First, we note that, in the leading term, ϵ_0 appears in the form of a product with $a_n^0 S_0/\xi_0$ (see Supplementary Information, Eq. (S23) for example), so that we chose $\epsilon_0 = 0.25$. Then, we tuned a_n^0/ξ_0 and a_p^0/ξ_0 to reproduce the experimental data of $\bar{v}_r^{\pm}(r)$. When the end-point confocal observation data #1 were used, we obtained $a_n^0/\xi_0 = 0.055$ μm^2/min and $a_p^0/\xi_0 = 0.8$ μm/min, with the results shown in Fig. 4(g) [see also Fig. S9(a) to (c)]. When the end-point confocal observation data #2 were used instead, we obtained $a_n^0/\xi_0 = 0.055$ μm^2/min and $a_p^0/\xi_0 = 1.4$ μm/min, with the results shown in Fig. S9(b) to (d).